THE JOURNAL OF PHYSICAL CHEMISTRY C

Article

pubs.acs.org/JPCC

On the Origin of the Enhanced Supercapacitor Performance of Nitrogen-Doped Graphene

Eunsu Paek, Alexander J. Pak, Kyoung E. Kweon, and Gyeong S. Hwang*

Department of Chemical Engineering, The University of Texas at Austin, Austin, Texas 78712, United States

Supporting Information

ABSTRACT: Graphene-based electrodes have been widely tested and used in electrochemical double layer capacitors due to their high surface area and electrical conductivity. Nitrogen doping of graphene has recently been demonstrated to significantly enhance capacitance, but the underlying mechanisms remain ambiguous. We present the doping effect on the interfacial capacitance between graphene and [BMIM][PF_6] ionic liquid, particularly the relative changes in the double layer and electrode (quantum) capacitances. The electrode capacitance change was evaluated based on density functional theory calculations of doping-induced electronic structure modifications in graphene, while the microstructure and capacitance of the double layers forming near undoped/doped graphene electrodes were calculated using classical molecular dynamics. Our computational study clearly demonstrates that nitrogen doping can lead to significant enhancement in the electrode capacitance as a result of electronic structure modifications while there is virtually no change in the double layer capacitance. This finding sheds some insight into the impact of the chemical and/or mechanical modifications of graphene-like electrodes on supercapacitor performance.

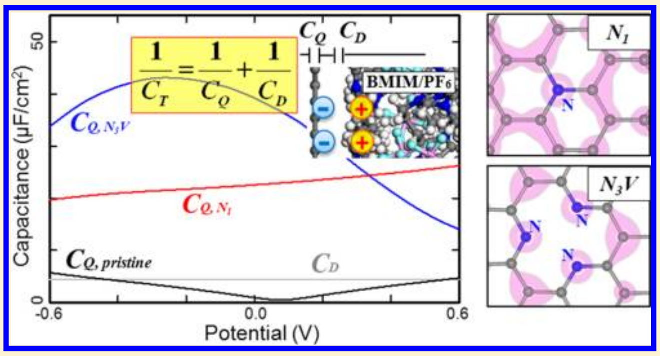

I. INTRODUCTION

Electrochemical double layer capacitors (EDLCs), also known as supercapacitors, have garnered much attention as electrical energy storage devices owing to their high rate capabilities and long cycle lifetimes.[1,2] Ionic liquids (ILs), "solvent-free" ions that are in the liquid state at room temperature, are a promising class of electrolytes due to their wide electrochemical windows, high chemical and thermal stability, extremely low volatility, and nonflammability.[3,4] Carbon-based materials (such as graphene, carbon nanotubes, and porous carbon) have been regarded as a viable candidate for supercapacitor electrodes due to their high specific surface area and good electrical conductivity.[1,5−9] However, a major drawback of EDLCs is their relatively low energy density compared to batteries;[1,2,5] hence, many efforts have recently been made to enhance the capacitor performance.[9−17]

Recent experiments have shown that nitrogen (N) doping of graphene-like electrodes can significantly enhance EDLC capacitance in comparison to undoped electrodes. Jeong and co-workers[14] reported a specific capacitance around 280 (225) F/g for N-doped graphene in KOH ([TEA][BF_4]), a 4-fold increase from the undoped graphene case; they claimed that the capacitance increase could be due to enhanced binding interactions between N dopants in the basal plane and electrolyte ions. Other researchers also showed that N-doped graphene can increase the capacitance to 144.6 F/g in KOH[15] (0.2 A/g), 144.9 F/g in [Et_4N][BF_4]/propylene carbonate[16] (0.5 A/g), or 326 F/g in KOH[17] (0.2 A/g). While the exact mechanisms remain ambiguous, the capacitance enhancements were thought to be related to an increase in the electrical conductivity of N-doped graphene[16] or the contribution of pseudocapacitance.[15,17] Among other possible factors, the important role of pseudocapacitance, together with EDL capacitance, in supercapacitors has been reported particularly when carbon-based electrodes include transition metal oxides;[18−23] the involvement of faradaic reactions (e.g., redox reactions or chemisorption) at the metal sites imparts additional capacitance beyond the double-layer capacitance.[24] For example, RuO_2 hydrates in aqueous solutions have been shown to change the valency state of Ru between Ru^{2+} and Ru^{4+} upon charge/discharge, which is balanced by electrochemical protonation.[18] In the case of MnO_2 hydrates, it has been shown that both protonation and chemisorption of cations in alkali and alkaline solutions occur upon changes in the valency state of Mn.[23]

While the interaction between dopants and electrolyte may influence the EDL capacitance, the total capacitance can also be affected by the doping-induced alteration of the electrode's capacitance. Recent experimental[25,26] and theoretical[27] work have shown that the total capacitance (C_T) of an IL/graphene-based electrode strongly depends on the relative contributions from both the double layer capacitance (C_D) and electrode

Received: December 19, 2012
Revised: February 14, 2013
Published: February 22, 2013

quantum capacitance (C_Q). The C_Q of low dimensional materials such as graphene is proportional to the electronic density of states (DOS),[28] which can be altered from chemical doping. To date, however, the effects of N doping on both C_Q and C_D have yet to be reported.

In this work, we investigate the influence of N doping of graphene in 1-butyl-3-methyl-imidazolium hexafluorophosphate ([BMIM][PF_6]) IL on the interfacial capacitance (C_T) using combined density functional theory (DFT) and classical molecular dynamics (MD) calculations. Our particular interest lies in understanding the relative contributions of EDL capacitance and quantum capacitance to the total interfacial capacitance in the N-doped case as compared to the undoped case. Here, charge transfer at the electrode/electrolyte interface, the so-called pseudocapacitance effect, is not considered since [BMIM][PF_6] is chemically inert. We have chosen to separately investigate two commonly observed N configurations from experimental[14,29] characterization: (1) substitutional N (N_1) in which a C atom is replaced with a N atom and (2) trimerized pyridine-type N (N_3V) in which three two-coordinated N atoms surround a C vacancy. We first employ DFT to predict the impact of each type on C_Q, which is proportional to the DOS.[27] We then consider the impact of N doping on the microstructure, potential variation, and C_D of the EDL using DFT/MD simulations. Finally, we compare the capacitance of the two N-doped cases to the undoped case.

II. COMPUTATIONAL METHODS

A. Density Functional Theory. The atomic and electronic structures of N-doped and pristine graphene sheets were calculated using DFT within the Perdew–Wang 91 generalized gradient approximation (GGA-PW91),[30] as implemented in the Vienna Ab initio Simulation Package[31] (VASP). We employed the projector augmented wave (PAW) method to describe the interaction between ion core and valence electrons,[32] and a planewave basis set with a kinetic energy cutoff of 400 eV. In this work, we considered two different N-doping configurations including single N atom substitution (referred to as N_1 hereafter) and trimerized pyridine-type (N_3V), as illustrated in Figure 1. The pristine/N_1 and N_3V graphene sheets were modeled using rectangular 32-atom (corresponding to 8.544 × 9.866 Å^2) and 112-atom (17.088 × 17.265 Å^2) supercells, respectively; here, the GGA-optimized lattice constant of 2.466 Å was employed, which is slightly larger than the experimental value of 2.461 Å. Periodic boundary conditions were employed in all three directions with a vacuum gap of 10 Å in the vertical (z) direction to separate the graphene system from its periodic images. For the Brillouin zone integration, we used a (12 × 12 × 1)/(6 × 6 × 1) Monkhorst–Pack mesh of k-points to determine the optimal geometries and total energies of the 32-atom/112-atom systems and sufficiently increased the k-point mesh size to ensure convergence of electronic structure calculations. The optimized structures for the N_1 and N_3V systems from our DFT-GGA calculations are presented in Figure 1; the predicted lattice distortions induced by N doping are in good agreement with previous calculation results.[33] N doping-induced changes in the atomic charge distribution of graphene were determined using grid-based Bader analysis.[34]

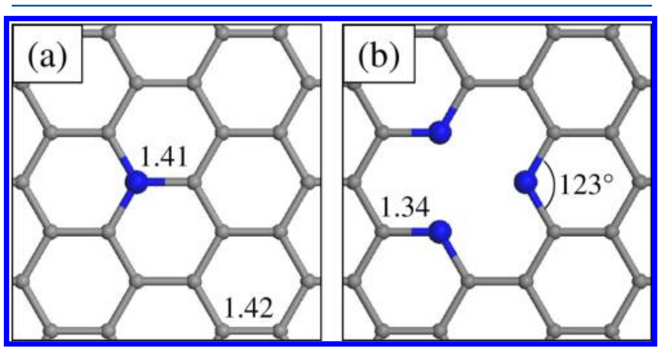

Figure 1. Schematic of (a) the substitutional nitrogen site (N_1) and (b) the trimerized pyridine- type nitrogen site (N_3V) considered in this work. Gray and blue balls are C and N atoms, respectively, and bond lengths are given in Å.

B. Classical Molecular Dynamics. We employed MD simulations with the OPLS-AA force field[35,36] to determine the microstructure of [BMIM][PF_6] near the graphene electrode; details on the force field parameters can be found in ref 27. As illustrated in Figure 2, the simulation system considered consisted of 346 [BMIM][PF_6] pairs between two electrodes separated by 100 Å; the lateral size of each graphene electrode was 34.18 × 34.53 Å^2, corresponding to 448 C atoms. The distance between the electrodes was chosen large enough such that the electrolyte maintained bulk properties in the middle region of the system.

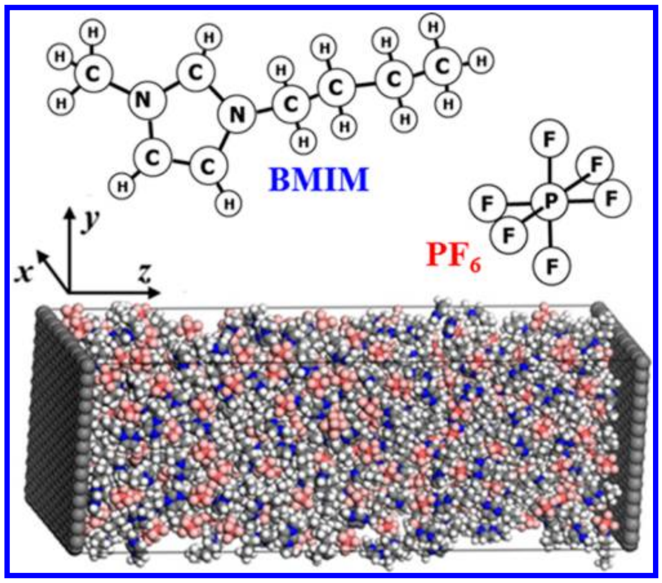

Figure 2. Schematic of BMIM, PF_6, and the simulation box. Planar graphene sheets are placed at the two ends of the simulation domain. White, blue, and gray balls indicate H, N, and C atoms in BMIM, and red and pink balls indicate P and F atoms in PF_6. Periodic boundary conditions are applied in the x and y directions.

For the N-doped graphene structures, 12 substitutional N atoms (corresponding to 2.7 at.% doping concentration) and 4 trimerized pyridine-type defects were distributed in the N_1 and N_3V graphene systems, respectively. We investigated uncharged and charged electrodes with a surface charge density of $\sigma = \pm$ 5.43 μC/cm^2. In the pristine graphene case, the atomic charges were assigned evenly throughout the lattice (±0.0089 e/atom when $\sigma = \pm$ 5.43 μC/cm^2). However in the N-doped cases, excess electrons/holes appeared rather concentrated around N atoms; in MD simulations, we used the atomic charge distributions from the Bader charge analysis for the N_1 and N_3V graphene systems (see Supporting Information, Table S1).

We ran each MD simulation initially at 1000 K for 1.2 ns followed by 3 ns at 300 K to equilibrate the system using a time step of 1 fs. Production runs were carried out for 4 ns with atomic positions recorded every 4 ps. All runs were in the NVT ensemble with the temperature controlled by a Nose–Hoover thermostat[37] with a 100 fs damping parameter. All MD simulations were performed with the Large-scale Atomic/Molecular Massively Parallel Simulator (LAMMPS) program.[38] MD results reported herein were obtained from the average of four independent simulations with different initial atomic configurations. Further details about the MD simulations are described in ref 27.

III. RESULTS AND DISCUSSION

The total interfacial capacitance (C_T) between graphene and [BMIM][PF_6] IL was computed from a series of the EDL capacitance (C_D) and the quantum capacitance of graphene (C_Q), i.e., $1/C_T = 1/C_D + 1/C_Q$. In the following sections, we present the calculations of C_Q and C_D, and based on the results, discuss their relative contributions to the C_T of the graphene/IL system.

A. Quantum Capacitance. The quantum capacitance of graphene is defined as $C_Q = d\sigma/d\phi_G$, where $d\sigma$ and $d\phi_G$ refer to the variations of charge density and local potential in graphene, respectively. Provided that the electrochemical potential μ of the graphene electrode is rigidly shifted by $e\phi_G$,[39] C_Q can be given by[27]

$$C_Q = e^2 \int_{-\infty}^{+\infty} D(E) F_T(E - \mu) dE \tag{1}$$

where $D(E)$ is the electron density of states (DOS), $F_T(E)$ is the thermal broadening function $[=(4kT)^{-1}\text{sech}^2(E/2kT)]$, E is the relative energy with respect to the Fermi level E_F, and e is the elementary charge.

For pristine graphene, the valence and conduction bands touch and both bands exhibit conical band dispersion near the Dirac point, where the Fermi level is located (Figure 3a). As also shown in Figure 3a, the calculated DOS of graphene using DFT-GGA is clearly demonstrated to be symmetric and linear near the Dirac point.

The electronic structure of graphene can be substantially altered by the presence of N impurities and/or C vacancies. Figure 3 also shows the band structure and DOS of N-doped graphene sheets considered. In the case of N_1 (single N atom substitution) graphene (Figure 3b), the Fermi level shifts up into the conduction band of pristine graphene due to electron injection into the π-electron system; note that N has one more electron than C, and thus each N → C substitution provides an extra electron to the graphene. The extra electron tends to spread rather broadly over the N atom and its neighboring C atoms, as demonstrated by the isosurface plot of the corresponding band-decomposed charge densities (Figure 3b). While the Fermi level position is a function of N concentration, at the 3.1 at.% doping level, there exists one partially filled defect state near the Fermi level; therefore, we can expect that the largely delocalized state will be first emptied (or filled) when extra holes (or electrons) are added (see the corresponding charge density isosurface plots in Figure 3b).

In the case of N_3V (trimerized pyridine-type) graphene (Figure 3c), the Fermi level moves down inside the valence band of pristine graphene due to electron deficiency; note that N_3V has one less electron than C_4 (defect-free graphene). At 2.7 at. % of N-doping, our band structure calculation shows the existence of three states near the Fermi level, that is, two degenerate quasi-localized states and one partially filled delocalized state. The distinct DOS peak at 0.05 eV below E_F is due primarily to the quasi-localized states associated with N lone pairs, as shown by the corresponding (band-decomposed) charge density isosurface plot. We can expect, therefore, that when excess holes are injected, the states associated with the N lone pairs will be emptied first.

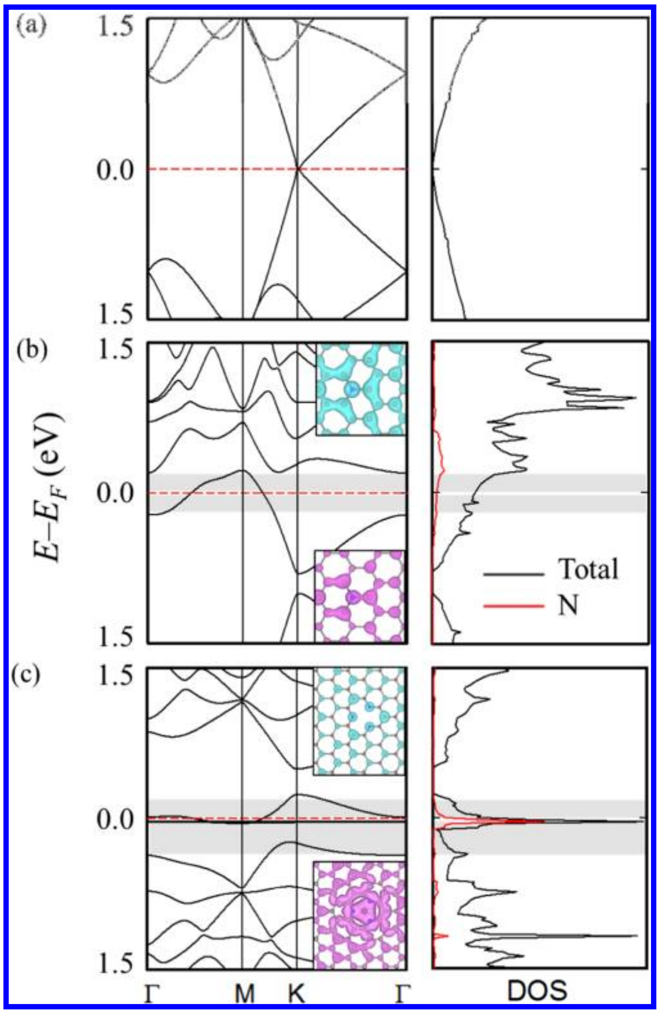

Figure 3. Band structures (left panels) and electronic density of states (right panels) for (a) pristine, (b) N_1, and (c) N_3V graphene. The dotted red line (left panels) indicate the Fermi level position. The insets (left panels) show the band-decomposed charge density isosurfaces ($\pm$0.0005 e/Å^3) for their respective shaded regions above and below the Fermi level.

Using eq 1 with the calculated DOS, we obtained the C_Q of the pristine, N_1, and N_3V graphene systems at 300 K, as presented in Figure 4. The C_Q of pristine graphene is U-shaped with a minimum around 0.45 μF/cm^2 at ϕ_G = 0 V. The C_Q for N_1 and N_3V at ϕ_G = 0 V are around 22 and 44 μF/cm^2, respectively; this dramatic improvement is apparently due to the additional impurity states near E_F. In the N_1 graphene case, C_Q gradually increases as ϕ_G increases and peaks at 45 μF/cm^2 at ϕ_G = 0.3 V. As ϕ_G decreases below 0 V, C_Q tapers toward 0 μF/cm^2 at −0.85 V. In the N_3V graphene case, C_Q sharply decreases to around 5−10 μF/cm^2 when ϕ_G < −0.2 V and 0 μF/cm^2 when ϕ_G = 0.4 V.

We have thus far presented an analysis pertaining to two ideal types of N doping in graphene; in reality, however, a

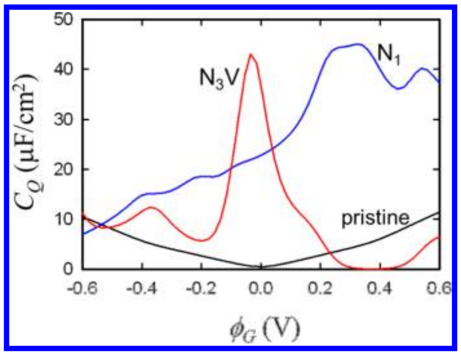

Figure 4. Comparison of the calculated quantum capacitance (C_Q) of pristine, N_1, and N_3V graphene as a function of the local electrode potential (ϕ_G).

fabricated N-doped graphene electrode may have numerous types of N-dopants and other possible structural defects.[14,29] In such a mixed system, the impact of the individual dopant types does not alter the electronic structure in simply an additive manner. Additional interactions between dopant types can also create unique states and alter the electronic structure (see Figure S5), but numerous combinations of these mixed dopants exist and are outside the scope of this study. We should also note that the possible influence of graphene-IL interactions on the DOS and C_Q have been neglected in this analysis for simplicity. However, it is clear that N-doping can lead to significant changes in the electrode capacitance.

B. Electric Double Layer Capacitance. The capacitance of an EDL can be obtained from the relationship between excess electrode surface charge (σ) and potential drop within the EDL (ϕ_D); that is, $C_I = \sigma/\phi_D$ (integral) or $C_D = d\sigma/d\phi_D$ (differential). We first calculated the integral capacitances at $\sigma = \pm$ 5.43 μC/cm^2 for the pristine, N_1, and N_3V graphene cases. For each system, the EDL capacitance was evaluated based on the microstructure of [BMIM][PF_6] IL near the electrified electrode determined using MD simulations, as described in the following section.

Figure 5 presents a comparison between the mass density profiles of BMIM and PF_6 at $\sigma = \pm$ 5.43 μC/cm^2 for pristine (a), N_1 (b), and N_3V (c) graphene. Each of the panels (a−c) displays an alternating cation/anion layering that extends 25−30 Å from the electrodes, after which the IL structure becomes nearly bulk-like; this layering behavior is consistent with previous experimental observations.[40−42] Near the positive electrode (z = 0 Å), PF_6 exhibits three distinct peaks adjacent to the electrode (in a−c); these peaks correspond to planarly aligned F, P, and F atoms, which arise primarily due to the electrostatic attraction between the positive electrode and the negatively charged F atoms. Near the negative electrode (z = 100 Å), the sharp peak (in a−c) corresponds to BMIM ions which tends to align parallel to the electrode surface.[43,44]

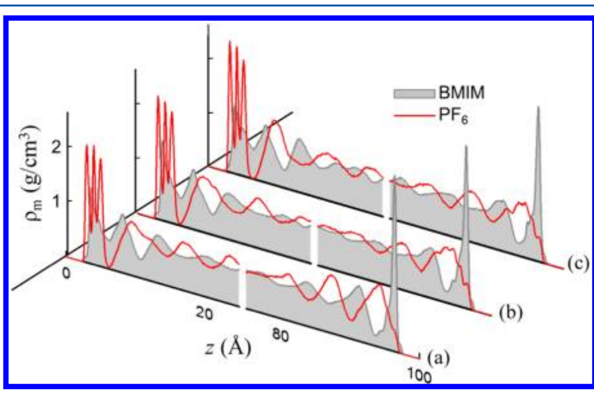

Figure 5. BMIM and PF_6 mass density (ρ_m) profiles for (a) pristine, (b) N_1, and (c) N_3V graphene systems along the z-axis. The positive (negative) electrode is located at z = 0 Å (100 Å).

The presence of N dopants and/or C vacancies affects the charge distribution throughout the electrode surface as stated earlier, which in turn influences the IL arrangement near the surface. In both N_1 and N_3V graphene cases, the positively charged BMIM rings have a tendency to lie near the negatively charged N atoms as a result of their electrostatic attraction (Figure S4). However, the influence of N doping on the IL distribution along the normal (z) direction appears to be insignificant (when the N concentration is about 2.7% as considered here); note that the average density of the first IL layer deviates at most by 3.3% compared to the undoped case.

For each system, the space charge variation in the IL electrolyte was calculated based on the distribution of IL ions with fixed atomic charges. We then obtained ϕ along the surface normal direction for a given σ from Poisson's equation

$$\varphi(z) = -\frac{\sigma z}{\varepsilon_0} - \frac{1}{\varepsilon_0}\int_0^z (z - z')\rho(z')dz' \tag{3}$$

where z is the distance from the electrode, ρ is the charge density averaged over a lateral z-cross section, and ε_0 is the vacuum permittivity.

Figure 6 shows a calculated potential profile for the pristine graphene case near the positive (left panel) and negative (right

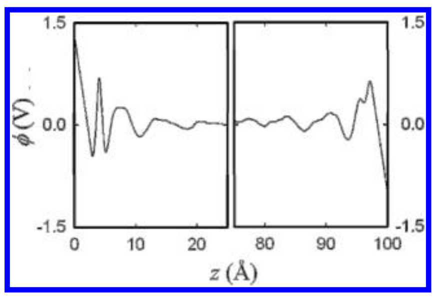

Figure 6. Potential (ϕ) profiles along the z-axis at $\sigma = \pm$ 5.43 μC/cm^2 for the pristine graphene system. The positive (negative) electrode is located at z = 0 Å (100 Å) and ϕ = 0 for the bulk electrolyte.

panel) electrodes with respect to the bulk potential (which is set equal to 0 V) for $\sigma = \pm$ 5.43 μC/cm^2. Here, a bin size of 0.1 Å was used in obtaining laterally averaged $\rho(z)$. The results show that the potential variation mostly occurs across the EDL, indicating that the accumulated counterions effectively screen the surface electric field. The ϕ_D near the positive (negative) electrode was 1.30 (−1.02) V. The potential profiles for the N_1 and N_3V graphene cases (not shown) are found to exhibit similarity to the pristine graphene case; the variation in ϕ_D among the three systems considered appears to be less than 5% (see Table 1).

In Table 1, we present the predicted C_I at σ = 0 and ±5.43 μC/cm^2 for each case. Note that in actuality, $C_I = \sigma/(\phi_D - \phi_Z)$,[45] where ϕ_Z is the potential of zero charge (which refers to the potential drop in the interface region due to a charge imbalance when σ = 0 μC/cm^2). For [BMIM][PF_6] near the intrinsic graphene sheet, the ϕ_Z is nearly zero (≈ 0.02 V). Similarly, the ϕ_Z for the N_1 and N_3V graphene cases are also

Table 1. Potential Drop across the EDL (ϕ_D) and Integral Capacitance (C_I) for Pristine, N_1, and N_3V Graphene Systems at $\sigma = \pm$ 5.43 $\mu C/cm^2$

	pristine	N_1	N_3V
		σ = +5.43 $\mu C/cm^2$	
$\phi_D - \phi_Z$ (V)	1.30	1.26	1.33
C_I ($\mu F/cm^2$)	4.18	4.30	4.09
		σ = −5.43 $\mu C/cm^2$	
$\phi_D - \phi_Z$ (V)	−1.02	−1.00	−1.05
C_I ($\mu F/cm^2$)	5.30	5.41	5.18

nearly zero (≈ 0.01 and 0.02 V, respectively). According to our calculations, the C_I values near the positive (negative) electrodes of 4.30 and 4.09 (5.41 and 5.18) $\mu F/cm^2$ for the N_1 and N_3V graphene systems, respectively, only slightly deviate from 4.18 (5.30) $\mu F/cm^2$ for the intrinsic case by at most 2.9%. This clearly suggests that N doping has little effect on the EDL capacitance at the N concentrations considered here (≈ 2.7% for both N_1 and N_3V graphene). Here, we should note that we neglect the possible polarization of graphene and IL ions at the interface and its effect on the electrode charge distribution, the space charge density, and the EDL capacitance, which merits further investigation. In addition, we cannot exclude the possibility that very high levels of doping might lead to noticeable deviations from the intrinsic case due to multiple factors, including possible specific adsorption of IL ions and enhanced interfacial electrostatic interactions.

C. Total Interfacial Capacitance. We attempted to evaluate the total interfacial capacitance (C_T, which is given as a series of the EDL capacitance and the quantum capacitance) as a function of applied potential (ϕ_a). Here, we considered the differential EDL capacitance (C_D) which is often preferred in investigating the properties of EDLs; the C_D is an indicator of how the EDL microstructure responds to potential perturbations caused by a variation in σ, and can be measured using low frequency impedance spectroscopy.[46]

Since N doping has no significant effect on the EDL capacitance, we only calculated the C_D for the intrinsic graphene case (which we assume is representative of both the N_1 and N_3V graphene cases). As shown in Figure 7, the

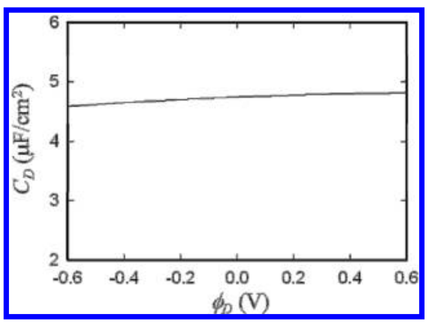

Figure 7. Differential double layer capacitance (C_D) as a function of the potential drop across the EDL (ϕ_D) for the pristine graphene system.

predicted C_D−ϕ_D curve is nearly flat for $|\phi_D|$ < 0.6 V with a maximum of 4.7 $\mu F/cm^2$ at ϕ_D = 0.7 V. Note that the peak position appears at a positive value of ϕ_D, which is related to the difference in packing efficiency between cation and anion.[27] That is, smaller PF_6 anions are more effectively packed than larger BMIM cations, yielding a smaller $\Delta\phi_D$ for a given $\Delta\sigma$ and consequently a larger C_D. Likewise, the C_D value monotonically decreases with increasing $|\sigma|$ (or $|\phi_D|$) due to the gradually reduced packing efficiency, while the PF_6 side consistently exhibits a higher C_D at a given $|\phi_D|$ than the BMIM side (not shown).

Figure 8 shows predicted C_T−ϕ_a curves for the pristine (b), N_1 (c), and N_3V (d) graphene systems, from the calculated C_Q

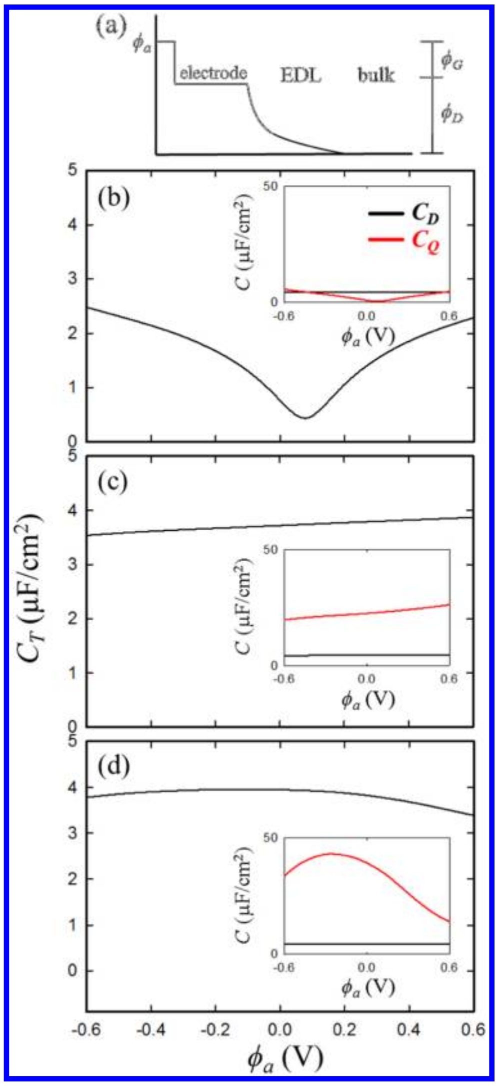

Figure 8. (a) Schematic of the idealized potential profile at the graphene/IL interface, and the total interfacial capacitance for (b) pristine, (b) N_1, and (c) N_3V graphene systems as a function of applied potential (ϕ_a).

and C_D above; recall $1/C_T = 1/C_Q + 1/C_D$. Here, as sketched in the Figure 8a, ϕ_a was assumed to be the sum of the local potential of the electrode (ϕ_G) and the potential across the EDL (ϕ_D), that is, $\phi_a = \phi_G + \phi_D$, while the bulk electrolyte was taken as a reference; the relationship between C_Q and C_D with ϕ_a was obtained through σ (recall that $C_Q/C_D \propto \sigma \propto \phi_G/\phi_D$). The predicted C_T−ϕ_a for pristine graphene is U-shaped, similar to its C_Q equivalent (inset Figure 8b), with a minimum near 0.5 $\mu F/cm^2$ at ϕ_a = 0 V. The C_T−ϕ_a curves for the N_1 and N_3V graphene systems also closely resemble their C_Q equivalents (insets of Figure 8c,d); recall that C_D is relatively flat when $|\phi_a|$ < 0.6 V such that it has little impact on the shape of the profile. Both C_T profiles for the N-doped cases show enhanced

dx.doi.org/10.1021/jp312490q | J. Phys. Chem. C 2013, 117, 5610−5616

capacitance in the range $|\phi_a| < 0.6$ V compared to the intrinsic case, which is in qualitative agreement with experimental studies;[14] it is apparent that this is due to the contribution from C_Q near $\phi_a = 0$ V. As mentioned above, however, this analysis only pertains to two ideal and probable types of N-doped graphene and does not extend toward systems with mixed N-dopant types. Nonetheless, our study clearly highlights that the enhanced capacitance observed in N-doped supercapacitors can be attributed to modification of the electrode capacitance.

IV. SUMMARY

We evaluated the interfacial capacitance of N-doped graphene in [BMIM][PF_6] IL using a combination of DFT and classical MD calculations, with particular attention to the relative contributions of the electrode and EDL capacitances. We considered two commonly observed N configurations from experiments, substitutional N (N_1) and trimerized pyridine-type N (N_3V). According to our DFT calculations, both types of N doping significantly tend to enhance the quantum capacitance of graphene near the Fermi level when compared to the undoped case; the N_1 graphene showed broad enhancement while N_3V graphene had sharp enhancement over a 0.4 V window. Our MD simulations for N_1 and N_3V graphene in [BMIM][PF_6] show that the positively charged BMIM rings have a tendency to lie near the negatively charged N atoms. However, the EDL microstructure and capacitance are found to be virtually unaffected at N doping concentrations of about 3 at. % considered in this work. In addition, the dependence of the total interfacial capacitance on voltage is strongly associated with the electrode capacitance when $|\phi_a| < 0.6$ V since the EDL capacitance is nearly constant in this voltage window. Our computational study clearly highlights that the enhanced capacitance observed in N-doped supercapacitors can be attributed to an increase in the electrode's capacitance. This finding may suggest that other structural and/or chemical modifications to graphene-based electrodes could significantly contribute to enhancing the performance of supercapacitors and warrants further investigation.

■ ASSOCIATED CONTENT

Supporting Information

Figures showing the mass density profiles with uncharged electrodes, the charge distribution on graphene as a result of N-doping, the configuration of ions near the doped electrodes, and the quantum capacitance as a result of mixed systems of N-dopants. This material is available free of charge via the Internet at http://pubs.acs.org.

■ AUTHOR INFORMATION

Corresponding Author

*E-mail: gshwang@che.utexas.edu.

Notes

The authors declare no competing financial interest.

■ ACKNOWLEDGMENTS

This work was supported by the R.A. Welch foundation (F-1535) and the U.S. Department of Energy, Office of Basic Energy Sciences, Division of Materials Sciences and Engineering (DE-SC001951). We would like to thank the Texas Advanced Computing Center for use of their computing resources. Helpful discussion with Rodney S. Ruoff is also greatly acknowledged.

■ REFERENCES

(1) Wang, G.; Zhang, L.; Zhang, J. A Review of Electrode Materials for Electrochemical Supercapacitors. *Chem. Soc. Rev.* **2012**, *41*, 797−828.
(2) Conway, B. E. *Electrochemical Supercapacitors: Scientific Fundamentals and Technological Applications*; Kluwar Academic: New York, NY, 1999.
(3) Rogers, R. D.; Seddon, K. R. Ionic Liquids—Solvents of the Future? *Science* **2003**, *302*, 792.
(4) Xu, W.; Angell, C. A. Solvent-Free Electrolytes with Aqueous Solution-Like Conductivities. *Science* **2003**, *302*, 422.
(5) Simon, P.; Gogotsi, Y. Materials for Electrochemical Capacitors. *Nat. Mater.* **2008**, *7*, 845.
(6) Lewandowski, A.; Galinski, M. Carbon−Ionic Liquid Double-Layer Capacitors. *J. Phys. Chem. Solids* **2004**, *65*, 281.
(7) Jiang, H.; Lee, P.; Li, C. 3D Carbon Based Nanostructures for Advanced Supercapacitors. *Energy Environ. Sci.* **2012**, *6*, 41.
(8) Wang, Y.; Shi, Z.; Huang, Y.; Ma, Y.; Wang, C.; Chen, M.; Chen, Y. Supercapacitor Devices Based on Graphene Materials. *J. Phys. Chem. C* **2009**, *113*, 13103−13107.
(9) Huang, X.; Qi, X.; Boey, F.; Zhang, H. Graphene-Based Composites. *Chem. Soc. Rev.* **2012**, *41*, 666−86.
(10) Garcia, B. B.; Candelaria, S. L.; Cao, G. Nitrogenated Porous Carbon Electrodes for Supercapacitors. *J. Mater. Sci.* **2012**, *47*, 5996−6004.
(11) Guo, H.; Gao, Q. Boron and Nitrogen Co-Doped Porous Carbon and Its Enhanced Properties as Supercapacitor. *J. Power Sources* **2009**, *186*, 551−556.
(12) Mishra, A. K.; Ramaprabhu, S. Functionalized Graphene Based Nanocomposites for Supercapacitor Application. *J. Phys. Chem. C* **2011**, *115*, 14006−14013.
(13) Li, Z. J.; Chang, T. X.; Yun, G. Q.; Jia, Y. Coating Single Walled Carbon Nanotube with SnO_2 and Its Electrochemical Properties. *Powder Technol.* **2012**, *224*, 306−310.
(14) Jeong, H. M.; Lee, J. W.; Shin, W. H.; Choi, Y. J.; Shin, H. J.; Kang, J. K.; Choi, J. W. Nitrogen-Doped Graphene for High-Performance Ultracapacitors and the Importance of Nitrogen-Doped Sites at Basal Planes. *Nano Lett.* **2011**, *11*, 2472−77.
(15) Jiang, B.; Tian, C.; Wang, L.; Sun, L.; Chen, C.; Nong, X.; Qiao, Y.; Fu, H. Highly Concentrated, Stable Nitrogen-Doped Graphene for Supercapacitors, Simultaneous Doping and Reduction. *Appl. Surf. Sci.* **2012**, *258*, 3438−43.
(16) Qiu, Y.; Zhang, X.; Yang, S. High Performance Supercapacitors Based on Highly Conductive Nitrogen-Doped Graphene Sheets. *Phys. Chem. Chem. Phys.* **2011**, *13*, 12554−58.
(17) Sun, L.; Wang, L.; Tian, C.; Tan, T.; Xie, Y.; Shi, K.; Li, M.; Fu, H. Nitrogen-Doped Graphene with High Nitrogen Level via a One-Step Hydrothermal Reaction of Graphene Oxide with Urea for Superior Capacitive Energy Storage. *RSC Adv.* **2012**, *2*, 4498.
(18) Zheng, J. P.; Jow, T. R. A New Charge Storage Mechanism for Electrochemical Capacitors. *J. Electrochem. Soc.* **1995**, *142*, L6.
(19) Pang, S.-C.; Anderson, M. A.; Chapman, T. W. Novel Electrode Materials for Thin-Film Ultracapacitors: Comparison of Electrochemical Properties of Sol-Gel-Derived and Electrodeposited Manganese Dioxide. *J. Electrochem. Soc.* **2000**, *147*, 444−50.
(20) Kuo, S.-L.; Wu, N.-L. Electrochemical Capacitor of $MnFe_2O_4$ with NaCl Electrolyte. *Electrochem. Solid-State Lett.* **2005**, *8*, A495.
(21) Kim, I.-H.; Kim, J.-H.; Cho, B.-W.; Lee, Y.-H.; Kim, K.-B. Synthesis and Electrochemical Characterization of Vanadium Oxide on Carbon Nanotube Film Substrate for Pseudocapacitor Applications. *J. Electrochem. Soc.* **2006**, *153*, A989.
(22) Kuo, S.-L.; Lee, J.-F.; Wu, N.-L. Study on Pseudocapacitance Mechanism of Aqueous $MnFe_2O_4$ Supercapacitor. *J. Electrochem. Soc.* **2007**, *154*, A34.
(23) Kuo, S.; Wu, N. Investigation of Pseudocapacitive Charge-Storage Reaction of $MnO_2 \cdot nH_2O$ Supercapacitors in Aqueous Electrolytes. *J. Electrochem. Soc.* **2006**, *153*, A1317.

(24) Conway, B. E.; Birss, V.; Wojtowicz, J. The Role and Utilization of Pseudocapacitance for Energy Storage by Supercapacitors. *J. Power Sources* **1997**, *66*, 1−14.
(25) Xia, J.; Chen, F.; Li, J.; Tao, N. Measurement of the Quantum Capacitance of Graphene. *Nat. Nanotechnol.* **2009**, *4*, 505−9.
(26) Stoller, M. D.; Magnuson, C. W.; Zhu, Y.; Murali, S.; Suk, J. W.; Piner, R.; Ruoff, R. S. Interfacial Capacitance of Single Layer Graphene. *Energ. Environ. Sci.* **2011**, *4*, 4685−4689.
(27) Paek, E.; Pak, A. J.; Hwang, G. S. A Computational Study of the Interfacial Structure and Capacitance of Graphene in [BMIM][PF_6] Ionic Liquid. *J. Electrochem. Soc.* **2013**, *160*, A1−A10.
(28) Luryi, S. Quantum Capacitance Devices. *Appl. Phys. Lett.* **1988**, *52*, 501.
(29) Zhao, L.; He, R.; Rim, K. T.; Schiros, T.; Kim, K. S.; Zhou, H.; Gutiérrez, C.; Chockalingham, S. P.; Arguello, C. J.; Pálová, L.; et al. Visualizing Individual Nitrogen Dopants in Monolayer Graphene. *Science* **2011**, *333*, 999−1003.
(30) Perdew, J. P.; Wang, Y. Accurate and Simple Analytic Representation of the Electron-Gas Correlation Energy. *Phys. Rev. B* **1992**, *45*, 13244.
(31) Kresse, G.; Furthmüller, J. Efficient Iterative Schemes for *Ab Initio* Total-Energy Calculations Using a Plane-Wave Basis Set. *Phys. Rev. B* **1996**, *54*, 11169.
(32) Blöchl, P. E. Projector Augmented-Wave Method. *Phys. Rev. B* **1994**, *50*, 17953.
(33) Fujimoto, Y.; Saito, S. Formation, Stabilities, and Electronic Properties of Nitrogen Defects in Graphene. *Phys. Rev. B* **2011**, *84*, 245446.
(34) Henkelman, G.; Arnaldsson, A.; Jónsson, H. A Fast and Robust Algorithm for Bader Decomposition of Charge Density. *Comput. Mater. Sci.* **2006**, *36*, 354−360.
(35) Jorgensen, W. L.; Maxwell, D. S.; Tirado-Rives, J. Development and Testing of the OPLS All-Atom Force Field on Conformational Energetics and Properties of Organic Liquids. *J. Am. Chem. Soc.* **1996**, *118*, 11225.
(36) Kaminski, G.; Jorgensen, W. L. Performance of the AMBER94, MMFF94, and OPLS-AA Force Fields for Modeling Organic Liquids. *J. Phys. Chem.* **1996**, *100*, 18010.
(37) Hoover, W. Canonical Dynamics: Equilibrium Phase-Space Distributions. *Phys. Rev. A* **1985**, *31*, 1695.
(38) Plimpton, S. J. Fast Parallel Algorithms for Short-Range Molecular Dynamic. *J. Comput. Phys.* **1995**, *117*, 1.
(39) John, D. L.; Castro, L. C.; Pulfrey, D. L. Quantum Capacitance in Nanoscale Device Modeling. *J. Appl. Phys.* **2004**, *96*, 5180.
(40) Mezger, M.; Schröder, H.; Reichert, H.; Schramm, S.; Okasinski, J. S.; Schöder, S.; Honkimäki, V.; Deutsch, M.; Ocko, B. M.; Ralston, J.; et al. Molecular Layering of Fluorinated Ionic Liquids at a Charged Sapphire (0001) Surface. *Science* **2008**, *322*, 424.
(41) Liu, Y.; Zhang, Y.; Wu, G.; Hu, J. Coexistence of Liquid and Solid Phases of Bmim-PF6 Ionic Liquid on Mica Surfaces at Room Temperature. *J. Am. Chem. Soc.* **2006**, *128*, 7456.
(42) Bovio, S.; Podesta, A.; Lenardi, C.; Milani, P. Evidence of Extended Solidlike Layering in [Bmim][NTf_2] Ionic Liquid Thin Films at Room-Temperature. *J. Phys. Chem. B* **2009**, *113*, 6600.
(43) Rivera-Rubero, S.; Baldelli, S. Influence of Water on the Surface of Hydrophilic and Hydrophobic Room-Temperature Ionic Liquids. *J. Phys. Chem. B* **2004**, *118*, 15133.
(44) Aliaga, C.; Baldelli, S. Sum Frequency Generation Spectroscopy and Double Layer Capacitance Studies of the 1-butyl 3-Methyl-imidazolium Dicyanamide-Platinum Interface. *J. Phys. Chem. B* **2006**, *110*, 18481.
(45) Bard, A. J.; Faulkner, L. R. *Electrochemical Methods: Fundamentals and Applications*, 2nd ed.; Wiley Interscience: New York, NY, 2000; p 541.
(46) Lockett, V.; Sedev, R.; Ralston, J.; Horne, M.; Rodopoulos, T. Differential Capacitance of the Electrical Double Layer in Imidazolium-Based Ionic Liquids: Influence of Potential, Cation Size, and Temperature. *J. Phys. Chem. C* **2008**, *112*, 7486.